Journal of Power Sources 248 (2014) 655–659

Contents lists available at ScienceDirect

Journal of Power Sources

journal homepage: www.elsevier.com/locate/jpowsour

Short communication

$LiMn_{1-x}Fe_xPO_4$ ($x = 0$, 0.1, 0.2) nanorods synthesized by a facile solvothermal approach as high performance cathode materials for lithium-ion batteries

Ye Hong, Zilong Tang*, Zijian Hong, Zhongtai Zhang

State Key Laboratory of New Ceramics and Fine Processing, School of Materials Science and Engineering, Tsinghua University, Beijing 100084, China

HIGHLIGHTS

- $LiMn_{1-x}Fe_xPO_4$ nanorods have been synthesized with high yield by a solvothermal route.
- Fe substitution at low concentration can greatly improve the electrochemical activity of $LiMnPO_4$.
- $LiMn_{0.8}Fe_{0.2}PO_4$ nanorods exhibit remarkable electrochemical properties.

ARTICLE INFO

Article history:
Received 21 July 2013
Received in revised form
9 September 2013
Accepted 26 September 2013
Available online 7 October 2013

Keywords:
Lithium manganese phosphate
Iron substitution
Solvothermal
Nanorods
Lithium-ion batteries

ABSTRACT

$LiMn_{1-x}Fe_xPO_4$ nanomaterials at low Fe concentration ($x = 0$, 0.1, 0.2) for lithium-ion batteries have been synthesized with high yield via a facile solvothermal route in a mixed solvent of water and polyethylene glycol (PEG200). SEM and TEM images reveal that all samples are single crystalline with similar rod-like shapes, and XRD characterizations indicate that the crystal lattices decrease with the increasing concentration of Fe. Electrochemical tests show that the best electrochemical properties can be achieved by substituting 20% of Fe at Mn-site. The as-prepared $LiMn_{0.8}Fe_{0.2}PO_4$ sample delivers a high initial discharge capacity of 165.3 mAh g^{-1} at 0.05C, which is close to the theoretical capacity of $LiMnPO_4$. Moreover, it also demonstrates excellent cycle performance and remarkable rate capability.

1. Introduction

Olivine structured $LiFePO_4$ has been intensively studied since the significant discovery of Goodenough et al. in 1997, due to its high specific capacity, low toxicity, low cost, and excellent thermal stability [1–3]. Nowadays, isostructural $LiMnPO_4$ has been considered as the next promising cathode material owing to the same theoretical capacity (170 mAh g^{-1}) and a higher potential plateau of 4.1 V vs. Li/Li^+ as compared with $LiFePO_4$ (3.45 V), which is expected to deliver higher energy density [4]. However, the inherent short-comings of $LiMnPO_4$, including low electronic conductivity and low lithium diffusion coefficient, lead to low specific capacity, poor rate capability, and poor cycle stability [4,5].

Many attempts have been made to enhance the electrochemical performance of $LiMnPO_4$: reducing the size of particles to the nanoscale [6–8], adding carbon coating to the surface [9,10], and doping with metal cations such as Mg^{2+}, Ca^{2+}, Fe^{2+}, Zn^{2+}, Ni^{2+}, Co^{2+}, Cu^{2+}, V^{3+}, Gd^{3+}, and Zr^{4+} [11–14]. Recently, substituting the Mn-site with Fe has been found to be extremely effective for improving the electrochemical performance. Previously, $LiMn_{1-x}Fe_xPO_4$ with high electrochemical performance has been obtained by substituting high concentration of Fe [15,16], but the energy density has been greatly decreased since the potential plateau of Fe^{2+}/Fe^{3+} in the olivine family is about 0.65 V lower than that of Mn^{2+}/Mn^{3+}. Therefore, the concentration of Fe substitution has to be as low as possible in order to achieve the maximum energy density [17].

As for the synthetic methods, solid-state techniques have been successfully used to prepare $LiMn_{1-x}Fe_xPO_4$, achieving up to 90% of the theoretical capacity at low rate and good cycle property at moderate rate [15,16,18]. Meanwhile, to the best of our knowledge,

* Corresponding author. Tel.: +86 10 62783685; fax: +86 10 62771160.
E-mail address: tzl@tsinghua.edu.cn (Z. Tang).

0378-7753/$ – see front matter © 2013 Elsevier B.V. All rights reserved.
http://dx.doi.org/10.1016/j.jpowsour.2013.09.123

liquid phase methods such as hydrothermal, solvothermal and sol–gel processes which can obtain materials of special morphology and uniform size [19–21], have yet to be fully developed. Although various nanostructured $LiMn_{1-x}Fe_xPO_4$ has been achieved by hydrothermal/solvothermal method previously, it still remains great challenge for its practical application due to the dissatisfactory electrochemical performance [22–24]. Recently, Some research groups have improved the electrochemical performance of $LiMn_{1-x}Fe_xPO_4$ by adding graphene as the growth matrix or using multi-step approaches [25,26]. However, the synthetic methods can't be applied to the actual production due to either expensive reagents or complicated procedures.

In the present work, we have improved the traditional solvothermal method by using the water–polyethylene glycol (PEG200) mixed solvent instead of the single organic solvent and successfully synthesized rod-like $LiMn_{1-x}Fe_xPO_4$ nanomaterials at low Fe concentration ($x = 0$, 0.1, 0.2) with high yield. The mixed solvent is helpful to improve the dispersion of the products by using PEG200 solvent, and also promotes the dissolution of the reagents and reduces the temperature of solvothermal reaction by adding water. The effect of Fe substitution on the crystal structure, morphology and electrochemical performance is investigated and discussed in detail. It has been confirmed that substituting 20% of Fe at Mn-site could exhibit the most improved electrochemical properties. Based on the attractive synthetic technology and the obtained high performance, our work may widen the future practical application of $LiMn_{1-x}Fe_xPO_4$ as cathode material for lithium-ion batteries.

2. Experimental

2.1. Preparation of materials

$LiMn_{1-x}Fe_xPO_4$ ($x = 0$, 0.1, 0.2) nanoparticles were synthesized by a simple solvothermal method with water-PEG200 (6:1, vol%) as the solvent mixture. Firstly, 90 mmol LiOH was dissolved in the water–PEG200 mixed solution, followed by adding 30 mmol H_3PO_4 to form a white suspension (solution 1). Meanwhile, 30 mmol $MnSO_4{\cdot}H_2O$ and $FeSO_4{\cdot}7H_2O$ were dissolved in deionized water with Mn/Fe molar ratios of 1/0, 9/1, and 8/2, and then 4.5 mmol ascorbic acid was added as the antioxidant (solution 2). Subsequently, solution 2 was introduced into solution 1 with drop-wise under continuous magnetic stirring. The above solution was stirred vigorously for another 20 min before transferred into a 100 ml Teflon-lined stainless steel autoclave. The autoclave was kept at 180 °C for 10 h in an oven, and then naturally cooled to room temperature. The as-obtained light-gray precipitate was filtrated, washed with deionized water and ethanol for several times, and dried at 80 °C in vacuum for 2 h. Finally, the as-prepared powders were mixed with 20 wt.% sucrose by ball milling for 12 h and heated at 700 °C for 10 h under the Ar atmosphere to yield carbon coating in order to improve the electrical conductivity of $LiMn_{1-x}Fe_xPO_4$.

2.2. Characterization of materials

Crystallographic structures of the as-prepared materials were characterized by power X-ray diffraction (XRD, Cu Kα, Rigaku D/max-V2500, Japan) from 15° to 65° (2θ) at 8° min^{-1}. In order to calculate the lattice parameters, five strong peaks above 40° were further measured with a step width of 0.01° at a step time of 3 s, and then refined by X'pert highscore software. Particle sizes, morphologies and microstructures were studied by scanning electron microscopy (SEM, LEO-1530, Germany) and transmission electron microscopy (TEM, JEOL-2011, Japan). Chemical composition of the as-prepared samples was determined by inductively coupled plasma analysis (ICP, Vista-MPX, USA) and carbon content was measured by elemental analyzer (CE-440, USA).

2.3. Electrochemical measurements

To fabricate the cathode, $LiMn_{1-x}Fe_xPO_4$ powders, polyvinylidene fluoride (PVDF), and Super P carbon black were mixed with a weight ratio of 80:10:10 in an N-methylpyrrolidinone (NMP) solvent. The obtained viscous fluid was cast on aluminum foil and dried at 110 °C in vacuum overnight. The film was rolled and cut into circular disks, and the loading of active material was 5–6 mg cm^{-2}. The electrode was assembled into a coin-type half cell (CR2032) with a lithium metal as counter electrode, a microporous polymer separator (Celgard 2400), and electrolyte of 1 M solution of $LiPF_6$ in ethylene carbonate/dimethyl carbonate (EC/DMC) (1:1, vol%). The test cell was assembled in an Ar-filled glove box.

The charge/discharge tests were carried out on LAND CT2001A system between 2.5 V and 4.5 V at room temperature. First the test cell was charged at the required rate (1C = 170 mA g^{-1}) to 4.5 V, and held at 4.5 V until the current decreased to 0.02C, and then discharged at the corresponding rate to 2.5 V. Electrochemical impedance spectroscopy (EIS) measurements were conducted in a frequency range of 100 kHz to 0.1 Hz, using CHI604B electrochemical workstation.

3. Results and discussion

Fig. 1a shows the XRD patterns of the as-prepared $LiMn_{1-x}Fe_xPO_4$ ($x = 0$, 0.1, 0.2). All of the identified diffraction peaks can be fully indexed to an orthorhombic structure of $LiMnPO_4$ with a *Pnma* space group, which are consistent with the reported values (JCPDS No. 74-0375). It is clear that no impurity phases can be detected. The three samples show very similar diffraction patterns, except for a slight shift of peaks to higher angles with substitution of Fe at Mn-site, as illustrated by the 311 peaks in the upper-right corner of Fig. 1a. The lattice parameters and unit-cell volume of the samples are compared in Table 1. The decrease in crystal lattice parameters and the shrink in cell volume can be found as increasing the concentration of Fe, since the ionic radii of Fe^{2+} (0.92 Å) is smaller than that of Mn^{2+} (0.97 Å) [27]. This change is approximately linear, as shown in Fig. 1b, which is in good agreement with Vegard's law. The above observations imply that Mn was successfully substituted by Fe to obtain a homogeneous $LiMn_{1-x}Fe_xPO_4$ solid solution. Moreover, the chemical composition of the as-prepared $LiMn_{1-x}Fe_xPO_4$ was determined by ICP analysis and the results are shown in Table 2. The mole ratio of Li:Mn:Fe:P is found to be a little deviation from the theoretical value, indicating that there might be some trace Mn compound resulting from the synthetic process. More systematic experiments for the structure of $LiMn_{1-x}Fe_xPO_4$ will be carried out in our future research.

Fig. 2a–c presents the SEM images of $LiMn_{1-x}Fe_xPO_4$ ($x = 0$, 0.1, 0.2) before carbon coating. All the samples are nanorods with 100–150 nm in thickness and 400–750 nm in length, which indicates that a small amount of Fe substitution does not change the morphology and size of $LiMnPO_4$. Moreover, it is observed that the rod-like nanostructures are of high yield and in uniform shape, leading this simple synthetic technology to be promising in future practical application. Elemental (CHN) analysis shows that the carbon content of $LiMn_{1-x}Fe_xPO_4$ ($x = 0$, 0.1, 0.2) after carbon coating is 3.71, 3.69, and 3.80 wt.%, respectively. As for $LiMn_{0.8}Fe_{0.2}PO_4$, little residual carbon can be observed around the surface of the nanorods (Fig. 2d), which is consistent with the elemental analysis results. Meanwhile, some longer nanorods were cut off into shorter ones due to the ball milling. $LiMn_{0.8}Fe_{0.2}PO_4$ sample was further characterized by TEM, HRTEM, and SAED, as shown in

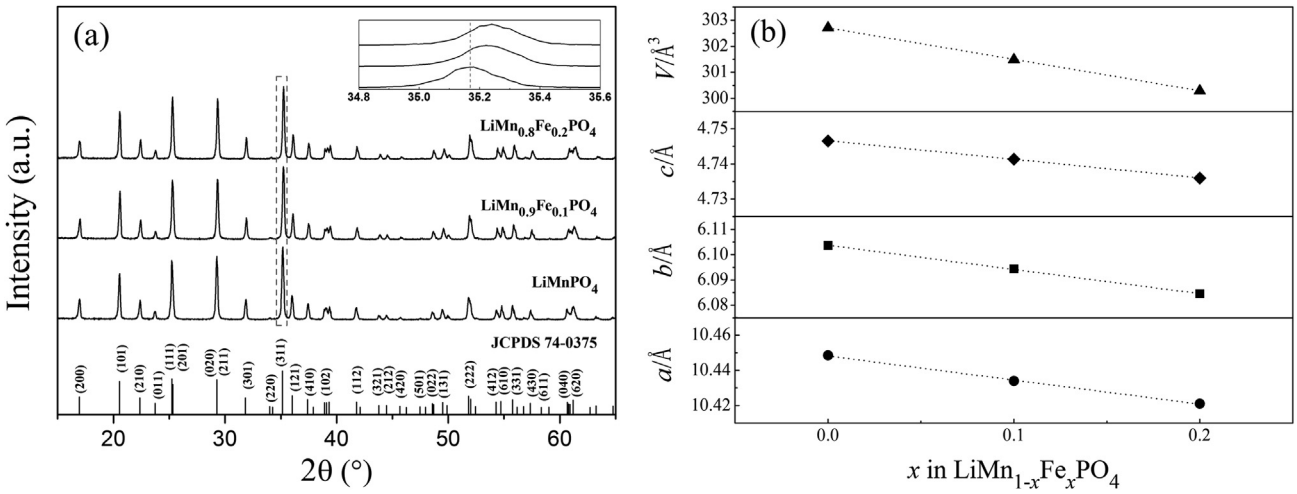

Fig. 1. (a) XRD patterns of $LiMn_{1-x}Fe_xPO_4$ samples. (b) Lattice parameters and unit-cell volume of $LiMn_{1-x}Fe_xPO_4$ as a function of iron concentration.

Fig. 3. TEM image (Fig. 3a) indicates that the sample is composed of nanorods with different lengths (coherent with Fig. 2d). From the HRTEM image (Fig. 3b), a thin amorphous carbon coating with the thickness of around 1.5 nm can be observed on the surface of the nanorod. The interplanar spacing of 3.697 Å can be identified as the (011) lattice plane of $LiMn_{0.8}Fe_{0.2}PO_4$. In addition, SAED patterns in Fig. 3c exhibit that the as-prepared sample is indeed single crystalline, and the SAED spots are in good agreement with the XRD pattern results shown in Fig. 1a.

The electrochemical properties of $LiMn_{1-x}Fe_xPO_4$ ($x = 0, 0.1, 0.2$) are compared in Fig. 4. Fig. 4a demonstrates the initial charge/discharge curves of the three samples at 0.05C (equal to 8.5 mA g^{-1}) at room temperature. $LiMn_{0.8}Fe_{0.2}PO_4$ nanorods deliver high initial specific discharge capacity of 165.3 mAh g^{-1}, which is close to the theoretical capacity of $LiMnPO_4$, while the discharge capacity of $LiMnPO_4$ and $LiMn_{0.9}Fe_{0.1}PO_4$ is only 84.1 mAh g^{-1} and 135.1 mAh g^{-1}, respectively. Moreover, the discharge potential plateaus corresponding to Mn^{2+}/Mn^{3+} gradually increases to 4.0 V vs. Li/Li^+ with increasing doping concentration of Fe, suggesting that the partial substitution of Fe at Mn-site can significantly enhance lithium ion diffusion and reduce polarization of $LiMnPO_4$. In addition, the $LiMn_{0.8}Fe_{0.2}PO_4$ sample shows two pairs of charge/discharge plateaus related to Mn^{2+}/Mn^{3+} and Fe^{2+}/Fe^{3+} redox couples in the 4.0 V and 3.5 V region, respectively. Theoretically, the length of the charge and discharge plateaus should be equal due to the almost same total capacity in charging/discharging process. However, the charge plateau is longer than the discharge plateau in the 4.0 V region, while the charge plateau in the 3.5 V region is shorter than the discharge one. This interesting phenomenon has been previously reported by Zhang et al. [28], and they found that the overpotential reached to the maximum in the transformation regions between the Fe^{2+}/Fe^{3+} and Mn^{2+}/Mn^{3+} redox couples. The maximum overpotential results in the minimum activation energy for phase transformation, so the charge/discharge plateaus in the 3.5 and 4.0 V region become asymmetric [29].

The cycling stability of the three samples at a charge/discharge rate of 0.5C is shown in Fig. 4b. $LiMnPO_4$ nanorods display the initial discharge capacity of 46.8 mAh g^{-1}, while $LiMn_{0.9}Fe_{0.1}PO_4$ exhibit 102.9 mAh g^{-1}. After charge/discharge for 70 cycles, the above two samples only remain in the low discharge capacity of 40.8 mAh g^{-1} and 76.6 mAh g^{-1}, which is 87.2% and 74.4% of the initial values, respectively. The decrease of capacities in the charge/discharge cycling can be attributed to the loss of electrochemical activity at Mn^{2+}/Mn^{3+} redox center with the higher content of Mn in olivine materials, which was reported in previous literature [27]. As for $LiMn_{0.8}Fe_{0.2}PO_4$ nanorods, they first deliver a discharge capacity of 125.8 mAh g^{-1}, but the capacity increases gradually and reaches the maximum value of 142.2 mAh g^{-1} at the 12th cycle. This abnormal observation was discussed by Saravanan et al. earlier [24], owing to the exposure of the surface of the active nanorods to the electrolyte. At the end of the 70th cycle, the reversible capacity of $LiMn_{0.8}Fe_{0.2}PO_4$ is found to be 131.6 mAh g^{-1} which is 92.5% of the maximum capacity at 12th cycle with a coulombic efficiency of 98.7%, suggesting that the as-prepared $LiMn_{0.8}Fe_{0.2}PO_4$ nanorods exhibit an excellent cycle performance at acceptable rate.

In order to further analyze the electrochemical kinetics of the above samples, EIS tests were conducted at the fully discharged state after 1st and 70th cycles at 0.5C, and the results are shown in Fig. 4c. All the spectra are similarly composed of one semicircle in the high-to-medium frequency range and a sloping line in the low frequency range. The impedance plots can be further explained by equivalent circuits (Fig. 4c inset). In detail, the intercept of the semicircle in high frequency corresponds to electrolyte resistance (R_e). The semicircle results from charge-transfer process and its diameter refers to charge-transfer resistance (R_{ct}), while constant-phase element (CPE) can be associated to the double-layer capacitance. The sloping line is related to Warburg impedance (Z_w), which is attributed to the solid state diffusion of lithium ion [30,31].

Table 1
Lattice parameters and unit-cell volume of as-prepared $LiMn_{1-x}Fe_xPO_4$ materials.

Sample	a (Å)	b (Å)	c (Å)	V (Å^3)
$LiMnPO_4$	10.448(4)	6.103(6)	4.746(5)	302.71
$LiMn_{0.9}Fe_{0.1}PO_4$	10.433(9)	6.094(3)	4.741(3)	301.49
$LiMn_{0.8}Fe_{0.2}PO_4$	10.421(0)	6.084(5)	4.735(9)	300.29

Table 2
Li:Mn:Fe:P atomic ratio of as-prepared $LiMn_{1-x}Fe_xPO_4$ materials determined by ICP analysis.

Sample	Measured stoichiometry			
	Li	Mn	Fe	P
$LiMnPO_4$	0.98	1.22	/	1
$LiMn_{0.9}Fe_{0.1}PO_4$	0.99	1.11	0.11	1
$LiMn_{0.8}Fe_{0.2}PO_4$	0.98	0.96	0.21	1

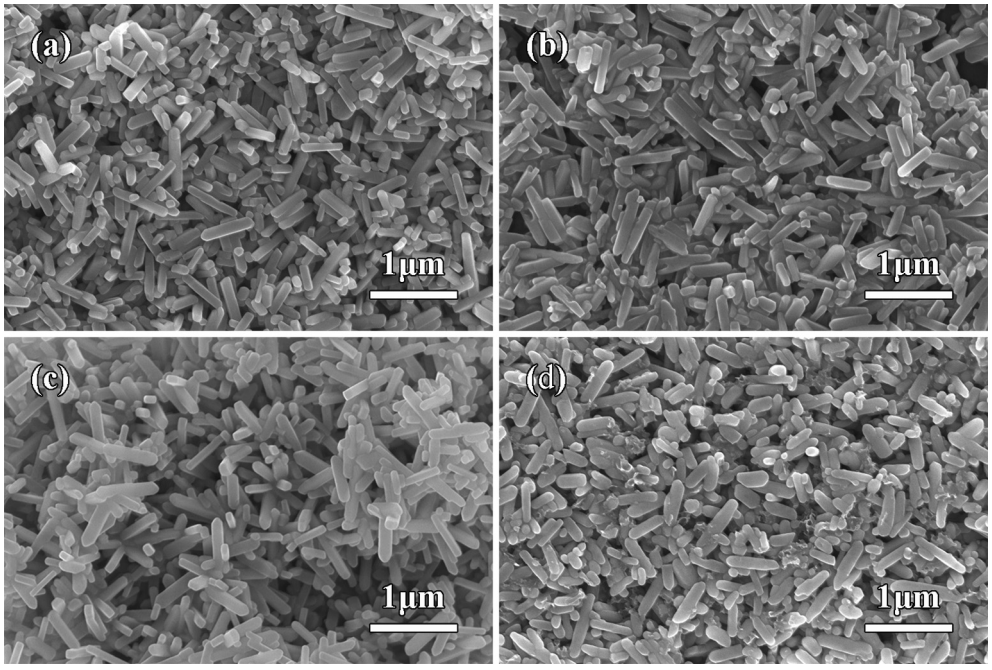

Fig. 2. (a–c) SEM images of $LiMn_{1-x}Fe_xPO_4$ materials before carbon coating: (a) $x = 0$, (b) $x = 0.1$, and (c) $x = 0.2$. (d) SEM image of $LiMn_{0.8}Fe_{0.2}PO_4$ after carbon coating.

It can be clearly observed that the semicircles of the Fe substituted samples are smaller than the original $LiMnPO_4$ at different cycles, indicating Fe substitution can really reduce the charge-transfer resistance of the electrochemical reaction. After the 70th cycle, $LiMn_{0.8}Fe_{0.2}PO_4$ nanorods exhibit the smallest charge-transfer resistance (~25 Ω) compared with other two samples (around 97 Ω of $LiMn_{0.9}Fe_{0.1}PO_4$ and even 124 Ω of $LiMnPO_4$), which is consistent with the highest discharge capacity as shown in Fig. 4b. Moreover, the charge-transfer resistance of $LiMnPO_4$ and $LiMn_{0.9}Fe_{0.1}PO_4$ drastically decreases after cycling, which can be attributed to the greatly improved contact between the active nanorods and the electrolyte [32]. However, the greatly improved penetration of the electrolyte in the active nanorods can also lead to more unexpected reactions such as Mn dissolution [33] and thus reduce the electrochemical activity of Mn^{2+}/Mn^{3+}, which is in accordance with the capacity decay upon cycling (Fig. 4b). As for $LiMn_{0.8}Fe_{0.2}PO_4$, the charge-transfer resistance shows a small reduction after cycling, corresponding to the increasing capacity in the first several cycles due to the improved exposure of the surface of the active materials to the electrolyte (Fig. 4b).

The rate capabilities of the as-prepared samples are also displayed in Fig. 4d. As expected, $LiMn_{0.8}Fe_{0.2}PO_4$ nanorods exhibit remarkable rate capability among three samples. The discharge capacity can reach as high as 160 mAh g^{-1} at 0.1C and even greater than 60 mAh g^{-1} at a high rate of 5C, which is superior to previously reported $LiMn_{1-x}Fe_xPO_4$ prepared by hydrothermal/solvothermal method [22,23]. All the analytic results confirm that 20% of Fe substitution at Mn-site can significantly enhance the electrochemical performance of $LiMnPO_4$.

4. Conclusions

We have successfully synthesized single-crystalline $LiMn_{1-x}Fe_xPO_4$ ($x = 0$, 0.1, 0.2) nanorods with high yield via a facile solvothermal route using water-PEG200 mixed solvent. It is found that Fe substitution leads to a decreasing crystal lattice and a shrink unit-cell volume but hardly affects the morphologies and particle sizes. Electrochemical measurements confirm that only a small amount of Fe concentration substituted at Mn-site can greatly improve the electrochemical properties. Especially $LiMn_{0.8}Fe_{0.2}PO_4$ nanorods exhibit highest reversible specific capacity (165.3 mAh g^{-1} at 0.05C), excellent cycle performance (131.6 mAh g^{-1} at 0.5C after 70 cycles), and remarkable rate capability (even above 60 mAh g^{-1} at 5C). The attractive simple synthetic technology and the obtained fascinating electrochemical properties make $LiMn_{1-x}Fe_xPO_4$ very competitive as cathode materials in future practical application.

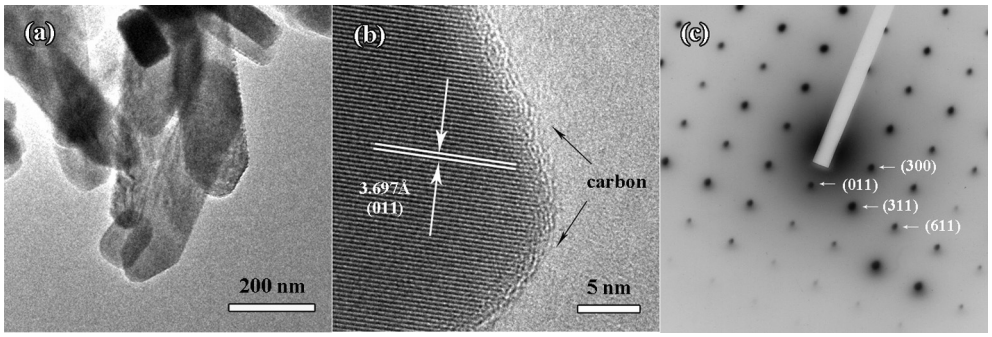

Fig. 3. (a) TEM, (b) HRTEM, and (c) SAED images of $LiMn_{0.8}Fe_{0.2}PO_4$ nanorods.

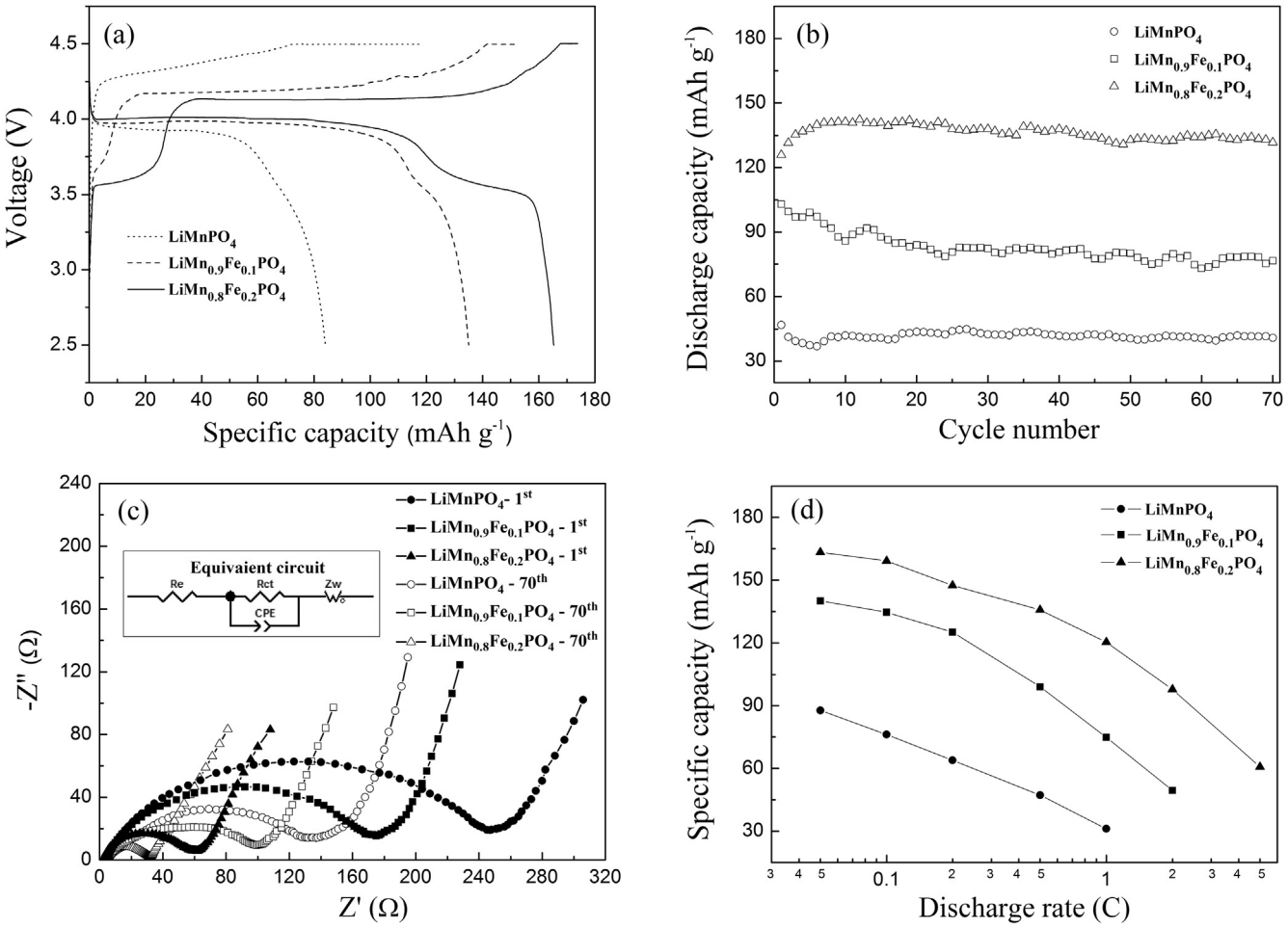

Fig. 4. (a) Initial charge/discharge profiles of $LiMn_{1-x}Fe_xPO_4$ nanorods at 0.05C. (b) Cycling performance curves of $LiMn_{1-x}Fe_xPO_4$ nanorods at 0.5C. (c) EIS plots of $LiMn_{1-x}Fe_xPO_4$ nanorods after 1st and 70th cycles at 0.5C in the frequency range of 100 kHz to 0.1 Hz. (d) Rate capabilities of $LiMn_{1-x}Fe_xPO_4$ nanorods as a function of cycle number.

Acknowledgments

This work is supported by the Doctoral Scientific Fund Project of the Ministry of Education of China (no. 20120002110007).

References

[1] A.K. Padhi, K.S. Nanjundaswamy, J.B. Goodenough, J. Electrochem. Soc. 144 (1997) 1188–1194.
[2] L.X. Yuan, Z.H. Wang, W.X. Zhang, X.L. Hu, J.T. Chen, Y.H. Huang, J.B. Goodenough, Energy Environ. Sci. 4 (2011) 269–284.
[3] W.J. Zhang, J. Power Sources 196 (2011) 2962–2970.
[4] M.K. Devaraju, I. Honma, Adv. Energy Mater. 2 (2012) 284–297.
[5] T. Shiratsuchi, S. Okada, T. Doi, J. Yamaki, Electrochim. Acta 54 (2009) 3145–3151.
[6] T. Drezen, N.H. Kwon, P. Bowen, I. Teerlinck, M. Isono, I. Exnar, J. Power Sources 174 (2007) 949–953.
[7] D. Rangappa, K. Sone, Y. Zhou, T. Kudo, I. Honma, J. Mater. Chem. 21 (2011) 15813–15818.
[8] J. Yoshida, M. Stark, J. Holzbock, N. Husing, S. Nakanishi, et al., J. Power Sources 226 (2013) 122–126.
[9] F. Wang, J. Yang, P. Gao, Y. NuLi, J. Wang, J. Power Sources 196 (2011) 10258–10262.
[10] J. Liu, X. Liu, T. Huang, A. Yu, J. Power Sources 229 (2013) 203–209.
[11] D. Wang, C. Ouyang, T. Drezen, I. Exnar, A. Kay, et al., J. Electrochem. Soc. 157 (2010) A225–A229.
[12] J.W. Lee, M.S. Park, B. Anass, J.H. Park, M.S. Paik, S.G. Doo, Electrochim. Acta 55 (2010) 4162–4169.
[13] J. Ni, L. Gao, J. Power Sources 196 (2011) 6498–6501.
[14] G. Yang, H. Ni, H. Liu, P. Gao, H. Ji, S. Roy, J. Pinto, X. Jiang, J. Power Sources 196 (2011) 4747–4755.
[15] D.H. Baek, J.K. Kim, Y.J. Shin, G.S. Chauhan, J.H. Ahn, K.W. Kim, J. Power Sources 189 (2009) 59–65.
[16] W. Liu, P. Gao, Y. Mi, J. Chen, H. Zhou, X. Zhang, J. Mater. Chem. A 1 (2013) 2411–2417.
[17] H. Fang, E. Dai, B. Yang, Y. Yao, W. Ma, J. Power Sources 204 (2012) 193–196.
[18] S.K. Martha, J. Grinblat, O. Haik, E. Zinigrad, T. Drezen, et al., Angew. Chem. Int. Ed. 48 (2009) 8559–8563.
[19] Z. Hong, Z. Tang, Y. Hong, H. Tang, Z. Zhang, Mater. Lett. 93 (2013) 226–229.
[20] P. Nie, L. Shen, F. Zhang, L. Chen, H. Deng, X. Zhang, CrystEngComm 14 (2012) 4284–4288.
[21] H. Xia, K.R. Ragavendran, J. Xie, L. Lu, J. Power Sources 212 (2012) 28–34.
[22] J. Xu, G. Chen, H.J. Li, Z.S. Lv, J. Appl. Electrochem 40 (2010) 575–580.
[23] K. Saravanan, J.J. Vittal, M.,V. Reddy, B.V.R. Chowdari, P. Balaya, J. Solid State Electrochem. 14 (2010) 1755–1760.
[24] K. Saravanan, V. Ramar, P. Balaya, J.J. Vittal, J. Mater. Chem. 21 (2011) 14925–14935.
[25] H. Wang, Y. Yang, Y. Liang, L.F. Cui, H.S. Casalongue, Y. Li, et al., Angew. Chem. Int. Ed. 50 (2011) 7364–7368.
[26] N.H. Kwon, K.M. Fromm, Electrochim. Acta 69 (2012) 38–44.
[27] G. Kobayashi, A. Yamada, S.I. Nishimura, R. Kanno, Y. Kobayashi, et al., J. Power Sources 189 (2009) 397–401.
[28] B. Zhang, X. Wang, H. Li, X. Huang, J. Power Sources 196 (2011) 6992–6996.
[29] M. Tang, H.Y. Huang, N. Meethong, Y.H. Kao, et al., Chem. Mater. 21 (2009) 1557–1571.
[30] A.V. Murugan, T. Muraliganth, A. Manthiram, J. Electrochem. Soc. 156 (2009) A79–A83.
[31] M. Zhao, G. Huang, W. Zhang, H. Zhang, X. Song, Energy Fuels 27 (2013) 1162–1167.
[32] B.Z. Li, Y. Wang, L. Xue, X.P. Li, W.S. Li, J. Power Sources 232 (2013) 12–16.
[33] Z. Tan, X. Wang, H. Zhou, Electrochim. Acta 90 (2013) 597–603.